Pharm Res (2015) 32:1304–1315
DOI 10.1007/s11095-014-1534-9

RESEARCH PAPER

Computational Fluid Dynamics Simulation of Hydrodynamics in USP Apparatus 3—The Influence of Dip Rate

Satish Perivilli • Maziar Kakhi • Erika Stippler

Received: 21 July 2014 / Accepted: 26 September 2014 / Published online: 19 November 2014

ABSTRACT

Purpose This study investigated the influence of dip rate on USP Apparatus 3 hydrodynamics in the presence of a solid dosage form (e.g. tablet) using Computational Fluid Dynamics (CFD) simulations. The primary variables of interest were the liquid phase velocity in the computational domain and wall shear stresses on the tablet surfaces.

Methods Geometry building and model setup were based on a number of simplifying assumptions. Computational grid-independent solutions were achieved for dip rates ranging from 5 to 10 dips per minute (dpm).

Results For all cases studied, the hydrodynamics exhibited a periodicity dictated by the dip rate. Cycle-to-cycle variations were found to be negligible. Higher velocities were predicted in the wake of the tablet and they peaked at midway positions both during the up- and downstrokes of the cylinder. Three sub-regions of velocity were identified inside the reciprocating cylinder. Results also showed localized vortices/recirculations specific to the up- and downstroke, in addition to local stagnation zones. The wall shear stresses and velocity magnitudes scaled proportionately with increasing dip rates while exhibiting qualitatively similar behavior in their spatial and temporal distributions.

Conclusions Based on the predictions of the 2D axisymmetric CFD model, the hydrodynamics in USP Apparatus 3 is characterized by complex and periodic flow structures.

KEY WORDS apparatus 3 · computational fluid dynamics · dissolution testing · hydrodynamics · wall shear stress

ABBREVIATIONS

C_2	Pressure jump coefficient (m^{-1})
C_v	Total liquid volume (m^3)
d	Tablet thickness (m)
d^*	Dimensionless axial coordinate of a point on the tablet side surface
h	Computational domain height (m)
h_c	Cylinder height (m)
h_l	Liquid level with submerged tablet (m)
N	Dip rate or rate of reciprocation (dpm)
OA	Open surface area of mesh screens
R	Tablet radius (m)
r	radial position/coordinate (m)
r^*	Dimensionless radial coordinate of a point on the tablet bottom and top surfaces
Re	Reynolds number
t	Physical time elapsed from start of process defined as cylinder position at the beginning of the upstroke (s)
t^*	Dimensionless time defined as ratio of time t, and time required for completion of two cycles of operation
U_n	Surface-normal fluid velocity (m/s)
U_z	Axial velocity of moving solid parts (m/s)
V	Tablet volume (m^3)
z	Axial position/coordinate (m)
z_0	Initial axial position of a point on the bottom mesh screen (m)
α	Porous surface permeability (m^2)
Δh_{bottom}	Distance between the bottom surfaces of the cylinder and vessel (m)
Δh_{top}	Distance between the top surfaces of the computational domain and the cylinder at the end of up stroke (m)
Δm	Porous surface thickness (m)
ΔP	Pressure drop across a porous surface (N/m^2)

Maziar Kakhi's Disclaimer: The views expressed in this paper are those of the authors and do not reflect the opinion nor the policy of the FDA.

S. Perivilli (✉) · E. Stippler
US Pharmacopeial Convention, 12601 Twinbrook Parkway, Rockville Maryland 20852-1790, USA
e-mail: svp@usp.org

M. Kakhi
Food and Drug Administration, Office of Testing and Research, 10903 New Hampshire Ave., Silver Spring, Maryland 20993, USA

μ	Liquid dynamic viscosity (kg/m-s)
ρ	Liquid density (kg/m^3)
τ_{bot} τ_{side}, τ_{top}	Wall shear stresses on the tablet bottom, side and top surfaces respectively (N/m^2)
Φ_c	Cylinder diameter (m)
Φ_v	Vessel diameter (m)
ω	Frequency of oscillation of moving solid parts (rad/s)

INTRODUCTION

USP Dissolution Apparatus 3, or the reciprocating cylinder apparatus (referred to as App 3 from here on), was incorporated into the *US Pharmacopeia* in 1991 [1] and is currently described in *USP* general chapter *Dissolution* <711> [2]. This apparatus was developed primarily for modified-release dosage forms to address the need for sequential modification of the composition of the dissolution medium and agitation rates in order to approach the goal of *in vitro–in vivo* correlation [3]. The apparatus consists of an outer flat-bottomed cylindrical vessel (referred to as *vessel* in this article) that contains the dissolution medium and a shorter inner cylinder (referred to as *cylinder* in this article) that reciprocates in and (partially) out of the vessel at a specified dip rate. An upstroke followed by a downstroke constitutes a single reciprocation cycle. Mesh screens with designated sizes are fitted at the top and bottom of the cylinder using caps. An evaporation cap is attached on the top of the vessel. The dimensions of the apparatus' components and allowable tolerances, as described in [2], are illustrated in Fig. 1. A solid dosage form is usually placed on the bottom screen of the cylinder, and the cylinder is dipped into dissolution medium at the beginning of a dissolution run. The dosage form stays within the dissolution medium throughout the reciprocation cycles.

The major factors that influence the dosage form's dissolution performance are its formulation, the dissolution media properties and the hydrodynamics to which it is subjected in the test apparatus. The design, mechanical setup and operation of a dissolution apparatus can alter the hydrodynamics of the system. The objective of this study was to understand the hydrodynamics in App 3 using CFD simulations.

CFD is a methodology for obtaining approximate numerical solutions to the conservation equations of mass, momentum, and energy for fluid flow problems. The use of CFD has been reported to model the fluid dynamics associated with USP Apparatus 2 [4–6] and USP Apparatus 4 [7, 8]. With respect to App 3, the scientific literature deals with experimental studies involving different solid dosage forms and the resulting dissolution profiles [3, 9–12]. The influence of geometrical and operational changes on the overall dissolution profiles has also been reported [9, 10]. However, no study known to the authors has focused on the hydrodynamics of the system. This study seems to be the first such attempt. The numerical models employed in this work present a simplified method to capture the hydrodynamics in App 3.

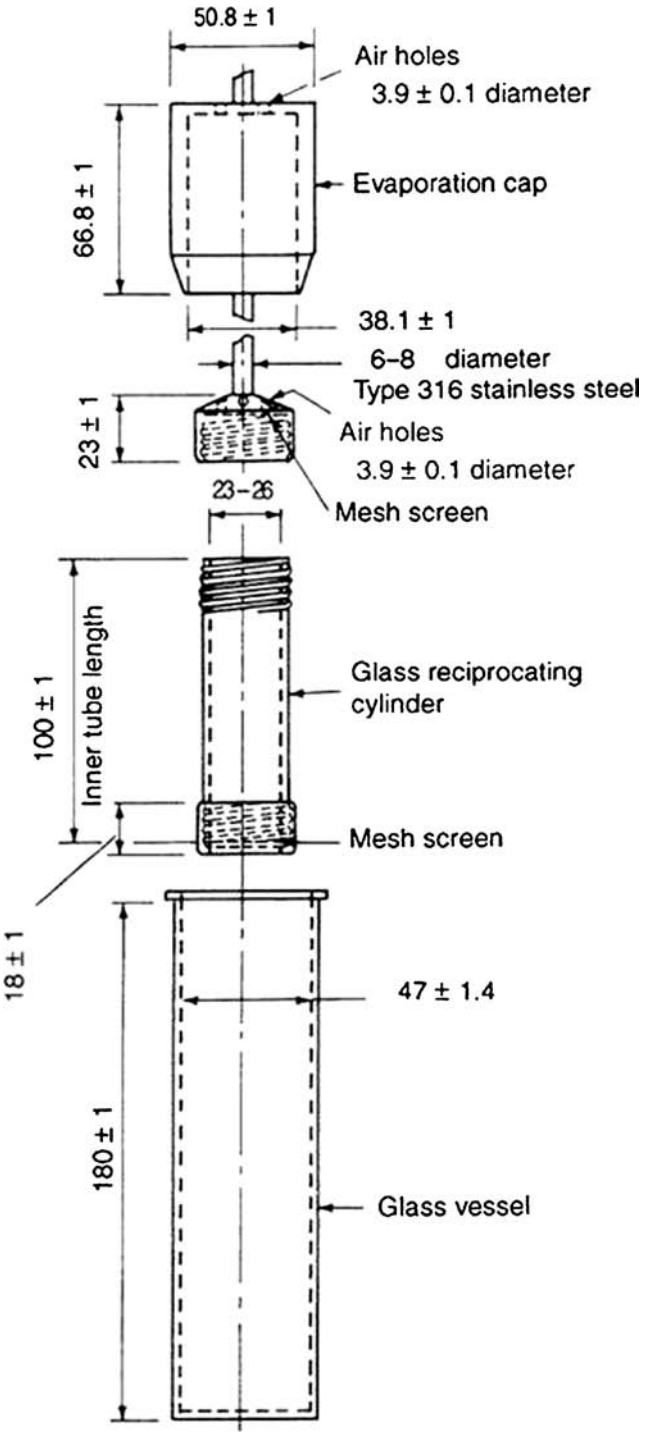

Fig. 1 A schematic of Apparatus 3. Reprinted with permission from [2]; all rights reserved.

MODEL DEVELOPMENT METHODS

App 3 hydrodynamics is primarily characterized by the reciprocating motion of the cylinder and the physical characteristics of its attached parts (such as screens and fitting caps). Modeling the reciprocation necessitates solution of unsteady flow equations with a moving grid which leads to extensive computational times. Therefore, a CFD model with manageable computational requirements was developed based on the following simplifications:

1. Temperature fluctuations throughout the system were considered negligible and therefore fluid viscosities and densities were assumed to be constant throughout the simulation. As a result, the evaporation cap was not modeled, and the solution of the energy equation was considered redundant.
2. A zero thickness cylinder wall was assumed and the top and bottom fitting caps were disregarded.
3. The top and bottom mesh screens were modeled as plane surfaces using porous jump boundary conditions.[1] In order to make use of a porous jump assumption, data relating the pressure drop across the mesh screens to the incoming fluid impact velocity are required. The use of this boundary condition obviates the need for a detailed geometric resolution of the screen. Thus, the size and complexity of the CFD model were reduced considerably.
4. In general, the dosage form may lose contact with the bottom mesh screen during the cylinder's downstroke while staying in contact with it during the upstroke. In this study, however, the dosage form was modeled to stay fixed and its center was symmetrically aligned with the axis of the reciprocating cylinder during both the up- and downstrokes. For modeling purposes, the bottom porous jump was defined as an annular cross-section between the tablet bottom surface (modeled with a wall boundary condition) and the cylinder wall.
5. The dosage form was chosen to be representative of a non-disintegrating tablet formulation. In addition, any possible changes in size and/or shape of the dosage form were neglected. In this work the dissolution of the drug from the dosage form was not considered.
6. Surface tension effects were not modeled as the region of focus was around the tablet and not in the vicinity of the free surface.
7. Based on the circular symmetry of the apparatus around the dip axis, 2D axisymmetry was invoked to simplify geometry construction, meshing, and reduce the computational time required for calculations.

[1] Hereafter the terms 'mesh screen', 'porous surface' and 'porous jump' are used in relation to the top and/or bottom mesh screens.

Determination of the Reynolds number (Re) is important for classifying the flow regime and hence for selecting an appropriate mixing model in CFD calculations (for example, [13]). For the present evaluation, the cylinder diameter (Φ_c) is an appropriate length scale and the maximum (axial) speed of the cylinder at the highest dip rate considered in this study (i.e. 10 dpm) provides the most conservative velocity scale (of approximately 52.4 mm/s). Based on these choices Re equals 1870. When compared to the critical Reynolds number of 2,300 for internal pipe flow [14], the flow conditions can be considered laminar for the range of dip rates (5–10 dpm) being investigated.

Computational Domain Sizing and Kinematics

The focus of this study was to understand the influence of changing dip rate on the apparatus hydrodynamics; consequently all geometric parameters were retained across the simulations. The vessel and cylinder dimensions were within the tolerances specified in [2]. Figure 2 shows a simplified App 3 configuration based on the previously presented assumptions. The black solid lines represent the position of the cylinder at the beginning of an upstroke (or at the end of its downstroke) while the dashed lines represent its position at the end of an upstroke. The blue lines indicate the physical vessel surfaces while the red lines are modeled surfaces used to confine the domain at its calculated height. Calculations for determining the liquid level and total height of the computational domain are presented next.

Liquid Level

The liquid level, h_l, corrected for the displacement of liquid volume resulting from the solid tablet volume, is given by:

$$h_l = \frac{C_v + V}{\pi \left(\frac{\Phi_v}{2}\right)^2} \tag{1}$$

where C_v, Φ_v, and V are respectively the liquid volume, the vessel diameter, and the volume of the submerged tablet. The volume of the solid cylinder does not appear in Eq. 1 because of the assumption of zero-thickness walls.

Computational Domain Height

In Fig. 2 Δh_{bottom} represents the distance between the bottom surface of the cylinder and vessel at the beginning position. USP general chapter <711>[2] specifies the nominal values for the cylinder height and its stroke length

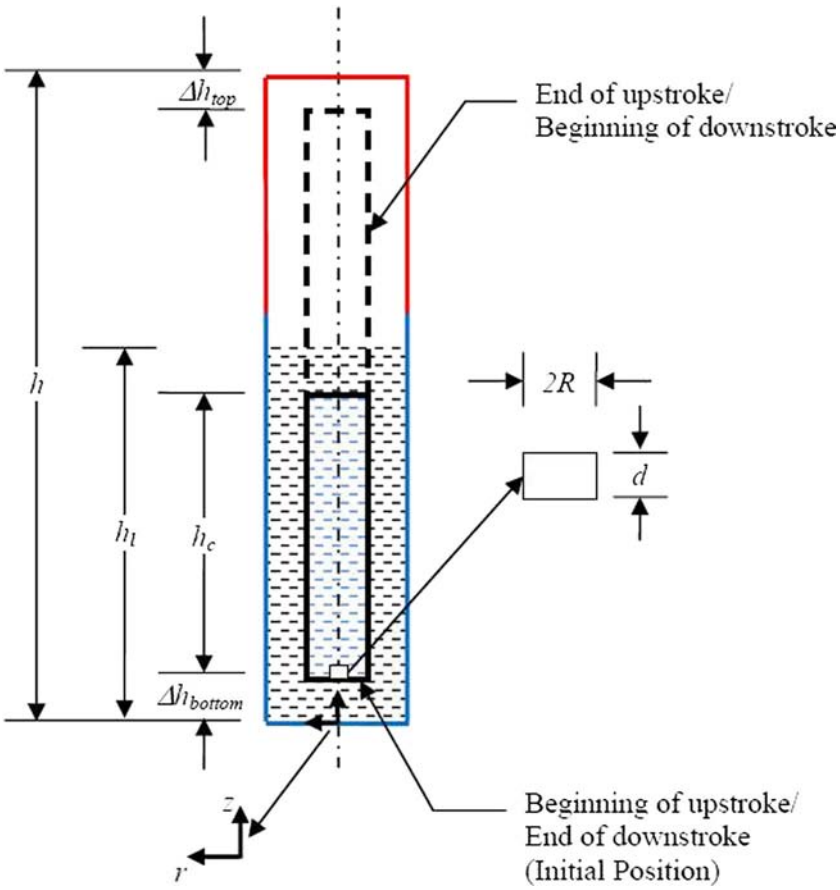

Fig. 2 Configuration employed for base calculations (refer Tables I and II for values).

to be equal, consequently the height of the computational domain can be expressed as:

$$h = 2h_c + \Delta h_{bottom} + \Delta h_{top} \tag{2}$$

where h_c is the cylinder height, and Δh_{top} is an assumed additional distance between the top surface of the computational domain and the cylinder at the end of an upstroke. The specification of Δh_{top} is required to enable the solver to predict a smooth transition of results since the boundary conditions associated with the moving cylinder and the top of the computational domain cannot be collocated. In addition, if Δh_{top} is assumed to be equal to Δh_{bottom} (and denoted Δh), then Eq. 2 reduces to:

$$h = 2\ (h_c + \Delta h) \tag{3}$$

The value of Δh_{bottom} was measured experimentally. The values for parameters used, and the resulting dimensions calculated, in Eq. 1 through Eq. 3 are shown in Tables I and II.

Motion Profile

USP general chapter <711> [2] does not specify an instantaneous motion profile for the cylinder. However, based on the most plausible profile, a sinusoidal wave form was used to define the translation of the cylinder, porous jump, and tablet surfaces. For simplicity, these three components are collectively referred to as 'moving solid parts' from here on. Considering a coordinate system with origin at the center of the vessel bottom surface, the axial coordinate of a point on the bottom mesh screen, z, at any time, t, is given by

$$z = z_0 + \frac{h_c}{2}\left[1 - \cos(\omega t)\right] \tag{4}$$

where z_0 (= Δh) is the initial position of that point. The frequency of oscillation (periodic reciprocating motion) ω was

Table I Vessel/Cylinder Characteristics used in Simulation from [2]

Characteristic	Value
Diameter of vessel, Φ_v	47 mm
Cylinder height, h_c	100 mm
Cylinder diameter, Φ_c	25 mm

Table II Sizing Characteristics of Computational Domain

Sizing Characteristic	Value
Total liquid volume, C_V	250 ml
Tablet radius, R	4.86 mm
Tablet thickness, d	4.5 mm
Computational domain height, h	224 mm
Liquid level in vessel accounting for tablet presence, h_l	144.29 mm
Distance between the bottom surface of the cylinder and vessel, Δh_{bottom}	12 mm
Distance between the top surface of the computational domain and the cylinder at the end of upstroke, Δh_{top}	12 mm

calculated as $2\pi N/60$, where N is the dip rate in units of dpm. The velocity in the axial direction is the time derivative of Eq. 4:

$$U_z = \frac{\omega\, h_c}{2}\sin(\omega t)\ . \tag{5}$$

This velocity profile was used to define the translation of the moving solid parts.

Preprocessing and Solver Specifications

Geometry, Boundary Conditions and Grid

Tools available within the ANSYS Workbench 13.0 environment were used to create the geometry and computational grids. Figure 3 shows the geometry and boundary conditions associated with it. As was mentioned previously, the top and bottom mesh screens were defined as porous jumps and the bottom mesh screen was considered to be adjacent to the tablet bottom surface. The computational domain was also divided into multiple sub-regions by means of the top and bottom interior surfaces between which the moving boundaries are located. At the top of the geometry only the pressure is known with confidence; consequently a pressure outlet condition for ambient air was assigned.

Various computational grids were generated with progressively reduced uniform sizes to evaluate grid-independence of the solution. Subsequently, additional grid refinement was performed only in the vicinity of the tablet surfaces using a combination of sphere of influence (SOI) and inflation methods. The SOI was specified with a radius of 10 mm centered on the midpoint of the tablet side surface. The grid inflation starting from the tablet surfaces was limited to a maximum of 25 layers with a growth rate of 1.05.

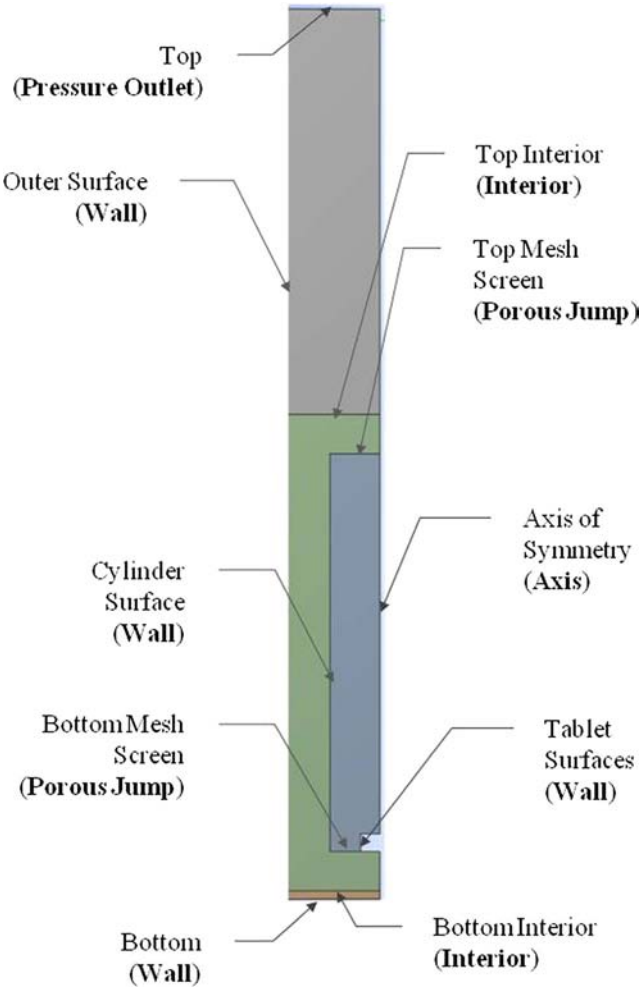

Fig. 3 Computational domain—geometry and boundary conditions.

Solution

The set of coupled and discretized partial differential equations describing the flow in App 3 was solved using the double precision ANSYS Fluent solver. A pressure-based transient analysis was set up with an absolute velocity framework. A first-order implicit scheme was used for the discretization of the time rate of change. Since the cylinder is initially fully immersed in water and during the upstroke moves partially into air surrounds, a volume of fluid (VOF) multiphase model was employed to model the free liquid surface exposed to air and the exchange of mass and momentum across it. Volume fractions at the air/water interface were determined using the geo-reconstruct scheme.

The porous jump conditions used for representation of the top and bottom mesh screens were characterized by means of a pressure drop given by:

$$\Delta P = \left(\frac{\mu}{\alpha}\, U_n + \frac{1}{2}\, C_2\, \rho\, {U_n}^2\right) \Delta m \tag{6}$$

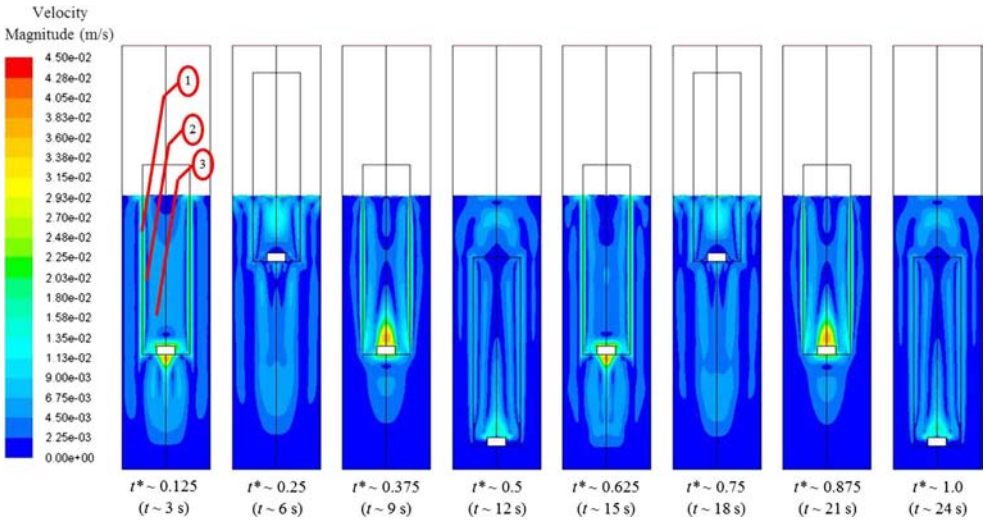

Fig. 4 Velocity magnitude contours in water domain at various time points for the 5 dpm case.

where μ and ρ are the dynamic viscosity and density, respectively, U_n is the fluid velocity in the direction normal to the surface, α is the porous surface permeability, and C_2 is a pressure jump coefficient [15]. The porous surface thickness, Δm, is the thickness of the actual mesh screen used with App 3 and was determined to be 1mm based on measurement. For perforated plates with various open surface areas, the relationship between pressure loss and uniform water impact velocity can be obtained from [16]. From [17], the open surface area (OA) for a screen with mesh size 20 is about 50%. Using information from [15–17], values of α and C_2 in Eq. 6 were estimated as 1.1E-9 m^2 and 2,669 m^{-1} respectively. Values of 993.75 kg/m^3 and 6.957E-4 kg/m-s were used for ρ and μ respectively in the calculations [18].

A "layering" scheme was used to achieve computational grid movement during the simulation. The region between the two interior surfaces (shown as the blue and green zones in Fig. 3), comprising the moving solid parts, was assigned a "rigid body" motion using the profile shown in Eq. 5. The remaining fluid zone (shown as grey and orange zones in Fig. 3) was also imparted the same "rigid body" motion per the software requirement. The axis and the outer surfaces of the computational domain, not within the interior surfaces, were allowed to "deform" (re-size) to accommodate the

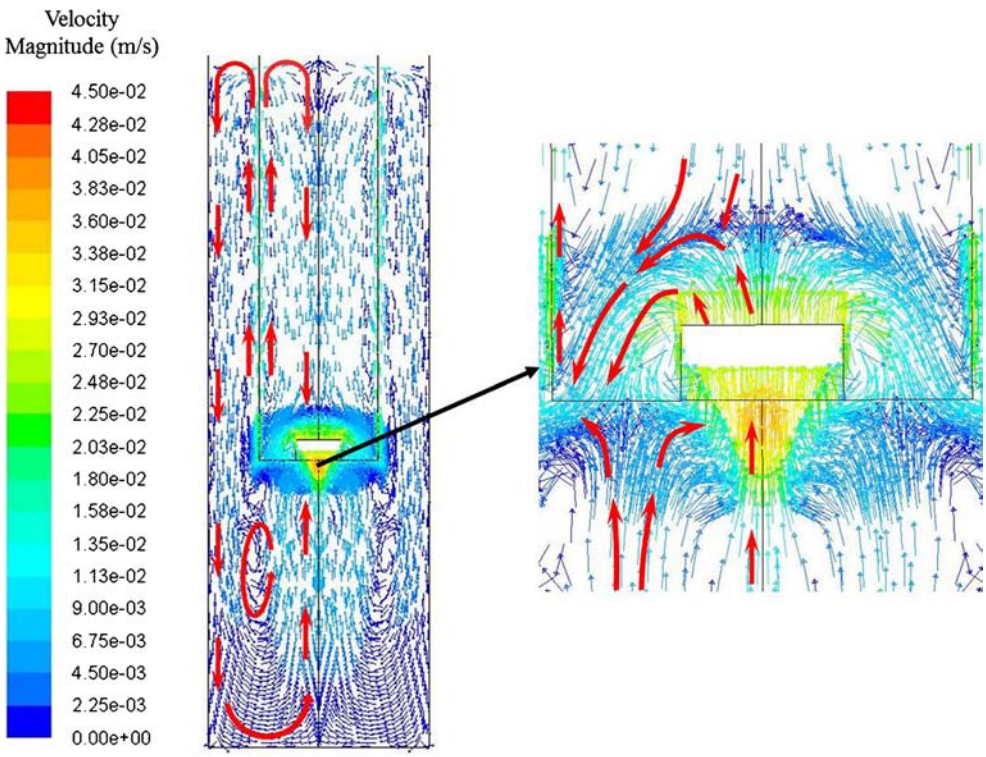

Fig. 5 Velocity magnitude vectors in water domain at $t^* \sim 0.125$ for the 5 dpm case (with local flow detail around the tablet).

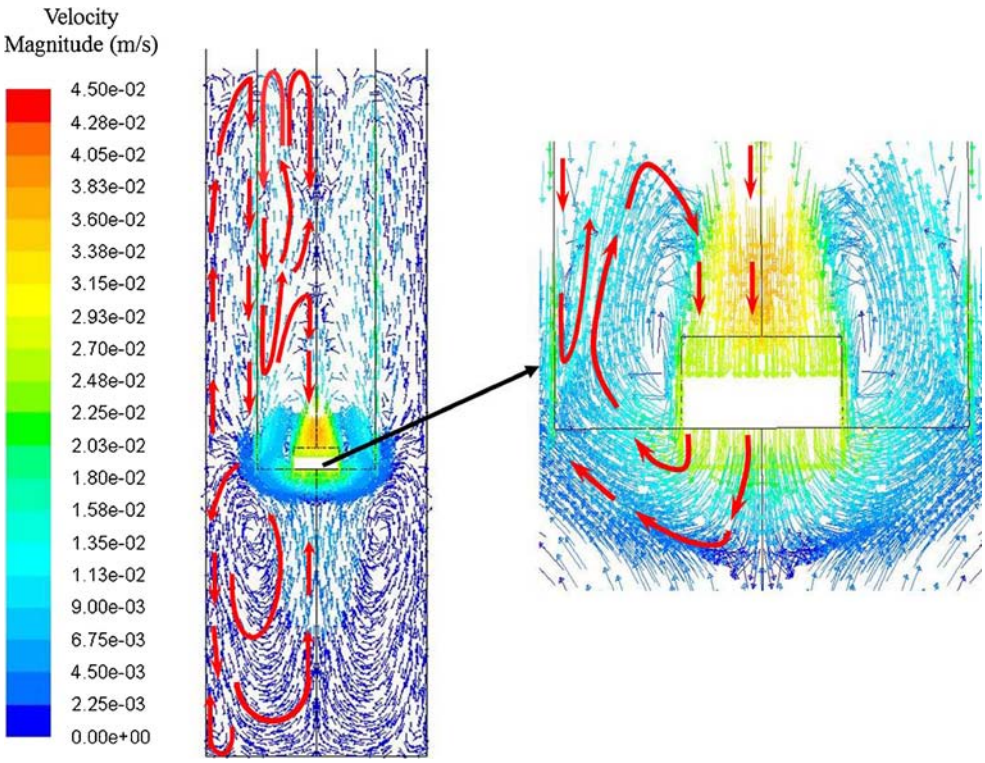

Fig. 6 Velocity magnitude vectors in water domain at $t^* \sim 0.375$ for the 5 dpm case (with local flow detail around the tablet).

dynamic grid of the moving zones. The bottom and top surfaces were modeled to be stationary.

The entire computational domain was initialized to contain air, and subsequently water was "patched" up to the liquid level shown in Fig. 2. A variable time-stepping scheme was used to solve the equations. The global Courant number was restricted to a maximum of 0.75 for all calculations. Simulations were performed for two full cycles for all dip rates considered. All simulations were carried out in parallel mode (using eight processors) on a Dell Precision T7500 workstation equipped with six dual-core Intel XEON 2.66 GHz processors and a total 24 GB of RAM.

RESULTS AND DISCUSSION

A comparison of results at 5 dpm showed that a grid size of 0.125 mm, SOI 0.03125 mm, and inflation with first layer thickness equal to 10^{-3} mm yields a grid-independent solution (assessed on the behavior of velocity magnitude and wall shear stresses at different locations in the computational domain). This grid contained 418,107 elements and the corresponding simulation required 24 h to complete. The initial, minimum, and maximum time steps were restricted to 10^{-3} s, 10^{-4} s, and 10^{-3} s (respectively) to ensure controlled mesh movement/layering. For this refined grid, results obtained with first- and second-order spatial discretization upwind schemes for solving momentum equations were found to be similar. All the results presented in this paper are based on grid-independent solutions.

The velocity magnitude contours (mirrored along the axis of symmetry) are presented in Fig. 4. The midway and the end positions of the up- and downstrokes for two cycles at 5 dpm are shown. Only the liquid phase (water) is presented. There is no change in liquid level in the vessel due to the zero wall thickness of the cylinder and continuous submergence of the tablet in the liquid phase. The dimensionless time, t^*, is defined as the ratio of time, t, to the time required for completion of two cycles. The results shown in Fig. 4 were sampled at approximate time points (as expressed by ~ sign) due to the variable time-stepping scheme used. The approximation was limited to one-half of the time step in progress.

The periodicity in the flow field at corresponding time points is apparent in Fig. 4 (e.g., results shown at $t^* \sim 0.125$ and $t^* \sim 0.625$ representing the midway positions on upstrokes in two consecutive cycles). Also, in general, the region inside the cylinder, away from the tablet, can be divided radially into three sub-regions based on velocity magnitude observations at any time point: a region of high fluid velocity along the cylinder wall (shown as region 1 in Fig. 4) due to the no-slip condition, an intermediate low velocity region in the close vicinity of the cylinder wall (region 2) and a broader high

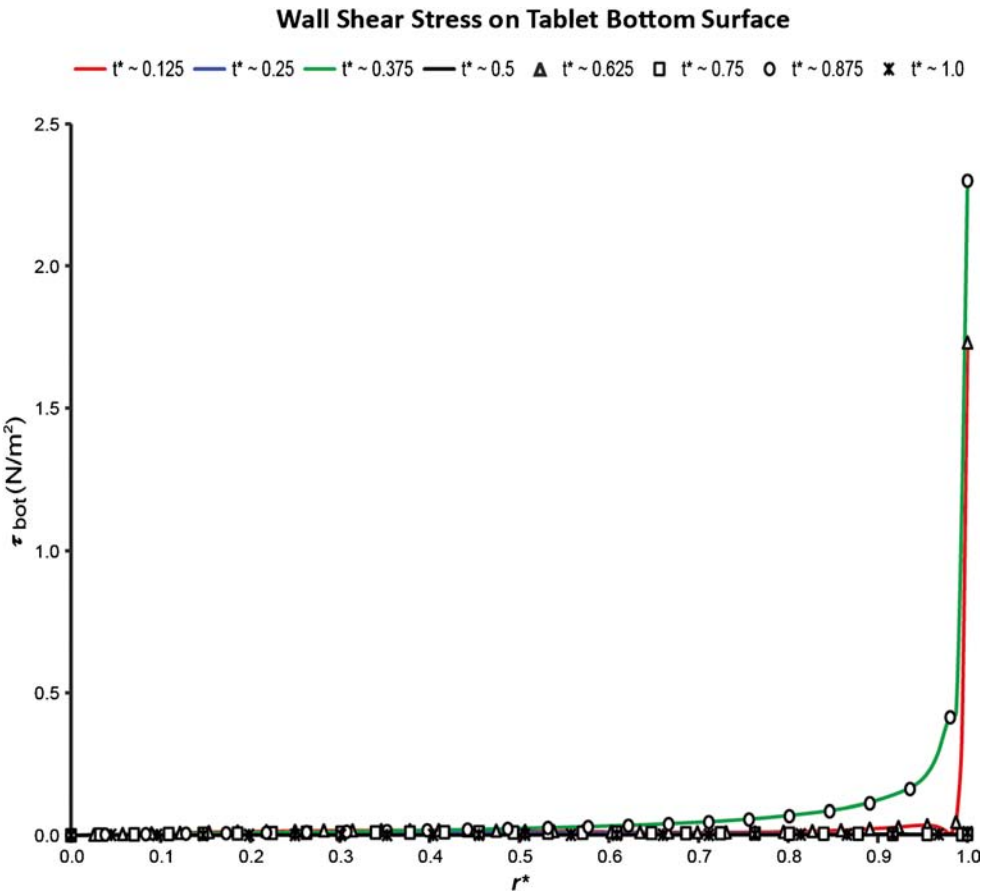

Fig. 7 Wall shear stresses on tablet bottom surface for the 5 dpm case.

velocity region along the center of the cylinder (region 3). Oppositely directed flows along the cylinder wall and near the cylinder axis result in a stagnation zone which manifests itself as the low velocity magnitudes predicted in region 2.

Figure 5 shows a vector plot of the velocity magnitudes in the liquid domain at $t^* \sim 0.125$ for the case with 5 dpm. The vectors are displayed with a fixed length in order to visualize all flow structures and in addition, guiding red arrows (on one-half of the axisymmetric domain) are included to represent major flow patterns. The upward movement of the tablet at $t^* \sim 0.125$ imparts an upward momentum to the fluid adjacent to it. This body of fluid impinges on downward directed flow structures further up the cylinder (near the axis of symmetry). The net effect is that the flow is steered towards the bottom corner of the cylinder, where a portion of it is picked up by the upward movement created by the cylinder and tablet side surface and the rest impinges on the porous surface.

The aforementioned downward directed flow structures form part of a large recirculation region inside the cylinder (as illustrated by the red arrow annotations in Fig. 5). This recirculation develops because the liquid adjacent to the cylinder wall has nowhere else to go once it approaches the liquid/air interface. Also, in the immediate wake of the tablet the highest velocity magnitudes were predicted as the fluid fills the space previously occupied by the tablet. The flow structures annotated in the cylinder region are also generally visible at the end of the upstroke ($t^* \sim 0.25$), albeit with much lower magnitude.

Figure 6 shows the velocity vector field during the middle of the downstroke ($t^* \sim 0.375$). The highest velocities are once again predicted in the wake of the tablet, which is now situated just above the top tablet surface. A local stagnation zone is created where the mass of upward-directed fluid in the containing vessel impinges on the downward-directed fluid just ahead of the tablet bottom surface (i.e. below the bottom porous screen). The recirculation 'bubbles' around the tablet are also notably bigger than during the upstroke partly because there is room for them to develop in this phase of movement; during the upstroke the mesh screen acted as a constraint on its size. As in the case of the upstroke, the salient flow structures present at $t^* \sim 0.375$ were also predicted at $t^* \sim 0.5$, albeit with lower magnitudes.

Wall shear stress distributions along the bottom, side and top tablet surfaces (τ_{bot}, τ_{side} and τ_{top}) respectively were also

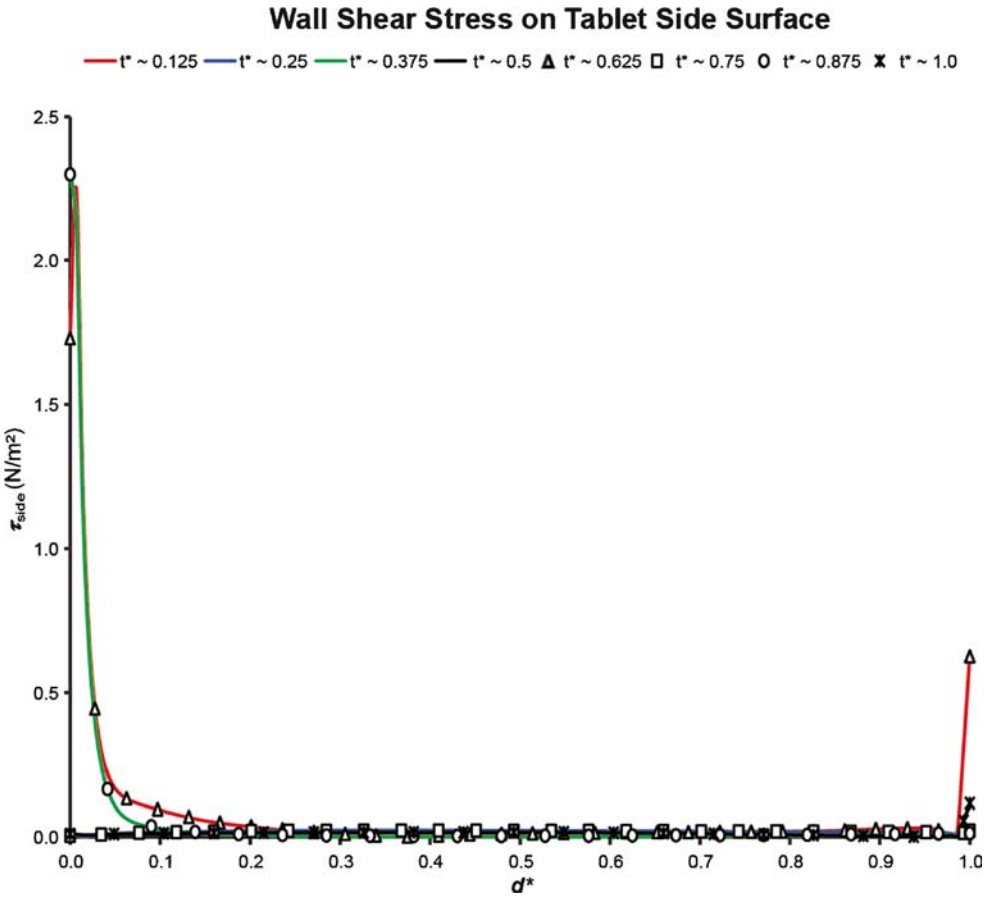

Fig. 8 Wall shear stresses on tablet side surface for the 5 dpm case.

analyzed and are shown in Fig. 7 through Fig. 9. In this model, the bottom mesh screen and the tablet bottom surface were adjacent. However, in reality, the tablet is placed on the bottom mesh screen and, as a consequence, the tablet bottom surface might experience a different wall shear stress profile than shown in Fig. 7. The dimensionless radial coordinate r^*, shown in Figs. 7 and 9, is the ratio of the radial coordinate of a point on the tablet surface (measured from the axis of symmetry) to the tablet radius, R. The dimensionless axial coordinate, d^*, in Fig. 8, is the ratio of the axial coordinate of a point on the side surface (measured from the tablet bottom) to the tablet thickness, d. Thus, the coordinates of (r^*, d^*) equal to (1, 0) and (1, 1) respectively represent the bottom-side and top-side corners of the tablet in the model.

Identical wall shear stress profiles were obtained at identical positions of the cylinder (for example, at $t^* \sim 0.125$ and $t^* \sim 0.625$) within the two cycles. τ_{bot} was the highest midway during the downstroke of a cycle, and τ_{top} was the highest during the upstroke. It was predicted that, in general, the central regions of all tablet surfaces (bottom, side, and top) experience low shear stresses. Higher shear stresses are predicted toward the edges of the top, bottom and side tablet surfaces.

The comparatively very low shear stresses predicted along the top and side sections of the tablet for $0 < d^* < 1$ and $r^* < 1$ are borne out by correspondingly low velocity gradients normal to the respective surfaces. Towards the edge of the tablet, the shear stresses are predicted to peak as the flow accelerates around it. In the particular case of the top tablet surface, the predominantly orthogonally-oriented flow over much of it leads to a very low shear stress component. For the tablet side surface, a well-developed boundary layer is not predicted to form; the simple model of a flow past a flat plate does not apply here as it is compounded by the effects of the side surface's short length and the sinusoidal time-dependence of its rigid body motion.

Figure 9 demonstrates a difference in the profiles of τ_{top} at midway positions during the upstroke ($t^* \sim 0.125$) and downstroke ($t^* \sim 0.375$). This can be explained by the velocity distribution towards the edge of the tablet ($r^* \sim 1$) at $t^* \sim 0.375$ being more uniform (i.e. near-zero gradients in the axial direction) compared to those at $t^* \sim 0.125$ as shown in Fig. 10. Also, on comparison, the tablet side surface is exposed to more identical flow conditions during both strokes of a cycle. Thus profiles of τ_{side} during the up- and downstrokes

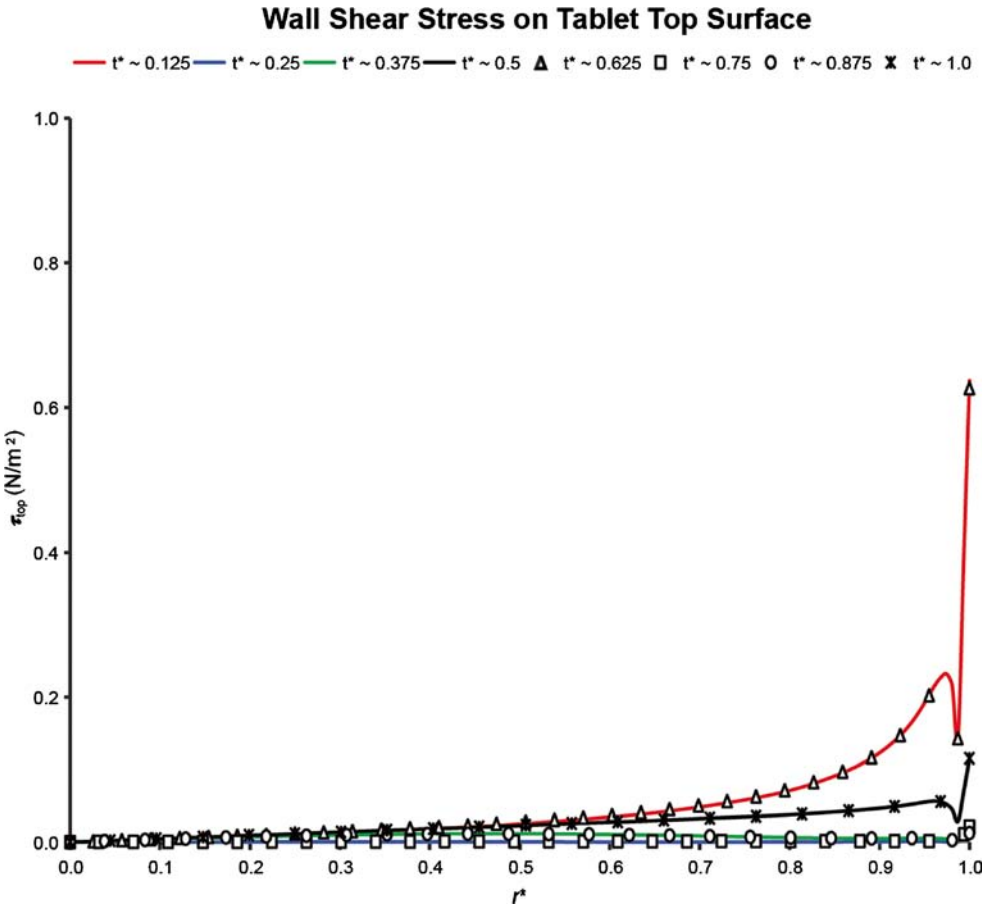

Fig. 9 Wall shear stresses on tablet top surface for the 5 dpm case.

were found to be comparable to each other, whereas those for τ_{bot} and τ_{top} showed differences.

Numerical solutions were also obtained for cases with dip rates of 5.25, 7.5 and 10 dpm. Generally, non-integer values for agitation speeds are not programmable in App 3. However, 5.25 dpm was simulated in order to evaluate the effect on the hydrodynamics within the acceptable compendial range (±5% of the stated agitation rate). The other rates were chosen to understand the influence of higher dip rates. The computational grid, solution methods and time steps from the 5 dpm case were retained.

Contours of velocity magnitude over the first cycle were compared across different dip rates in Fig. 11. From this figure it is apparent that the impact of increasing dip rate led to an expansion of the high-velocity regions inside and below the cylinder. In addition, the differences between the 5 dpm and 5.25 dpm results appear to be minor. The ratios of the maximum wall shear stresses at various dip rates to the maximum wall shear stresses at 5 dpm are presented in Table III. These ratios enable a better understanding of the influence of dip rates on the wall shear stresses experienced by the tablet surfaces. All maxima corresponded to the same location on the respective surface and at respective time points for all dip

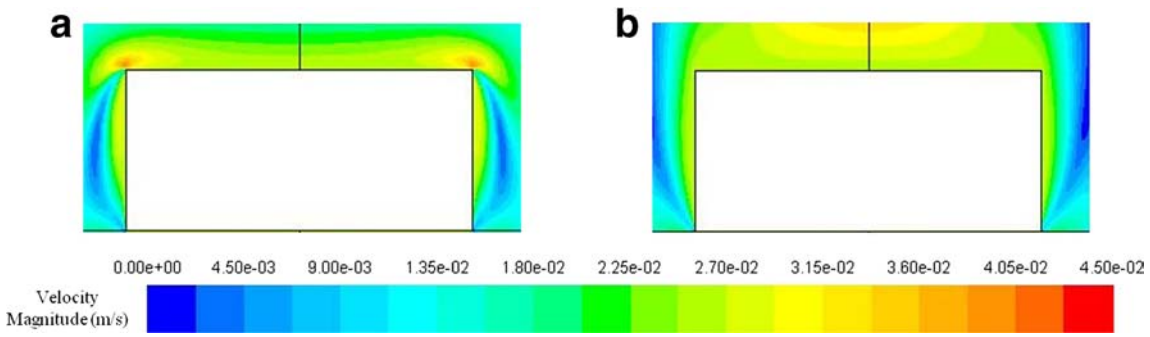

Fig. 10 Velocity magnitude distribution around the tablet top and side surfaces at (a) $t^* \sim 0.125$ and (b) $t^* \sim 0.375$ for the 5 dpm case.

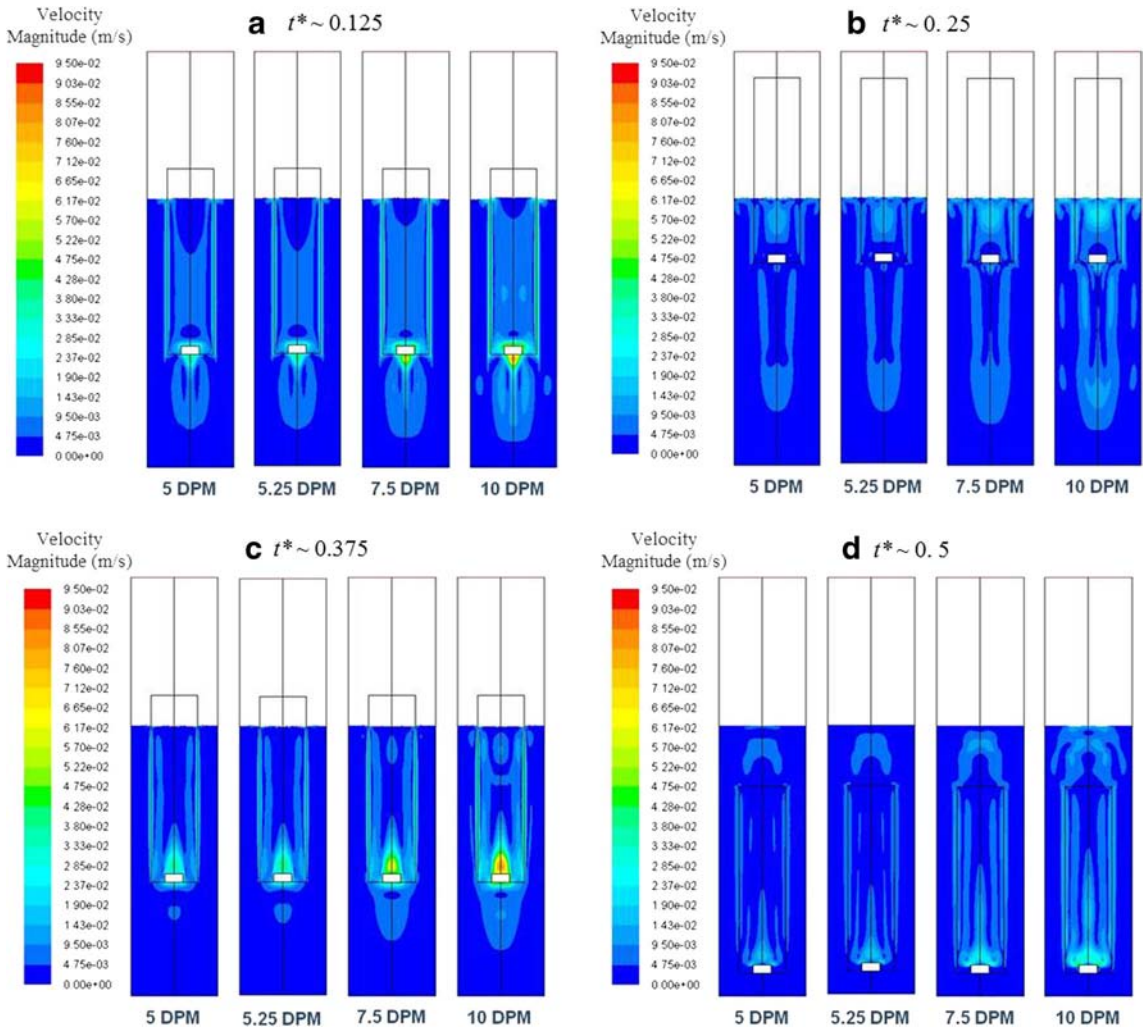

Fig. 11 Comparison of velocity magnitude (m/s) contours for cases with various dip rates.

rates. The ratios of wall shear stress maxima experienced by the tablet surfaces were found to be proportional to the ratios of change in dip rate. For example, an increase in dip rate from 5 to 10 dpm led to a corresponding increase of in the wall shear stress by a factor of 2.0–2.6. Furthermore, an increase of 5% led to only about 5% increase in wall shear stress maxima. However, it should not be inferred that the state of hydrodynamics in App 3 is being characterized by these ratios.

CONCLUSIONS

The results show complex flow structures that change as a function of time. Irrespective of the dip rate, the highest velocities were predicted in the wake of the moving tablet, and these were observed to peak at midway positions on both strokes of the cylinder. Three sub-regions of velocity were identified inside the reciprocating cylinder. Results also

Table III Influence of Dip Rate on Instantaneous Wall Shear Stress Maxima

Surfaces	Ratios of Wall Shear Stress Maxima (in Comparison to 5 dpm) for					
	10 dpm (at $t^*\sim0.125$)	7.5 dpm	5.25 dpm	10 dpm (at $t^*\sim0.375$)	7.5 dpm	5.25 dpm
Tablet Bottom	1.994	1.509	1.052	2.255	1.602	1.056
Tablet Side	2.053	1.533	1.048	2.255	1.601	1.056
Tablet Top	2.574	1.758	1.067	[a]	[a]	[a]

[a] Values for the top surface at $t^*\sim0.375$ were not included because of their near-zero magnitude

showed localized vortices/recirculations specific to the up- and downstroke, in addition to local stagnation zones. Comparison of results at increasing dip rates showed an increase in the velocity magnitude maxima. However, the same major qualitative flow features were predicted with changing dip rates.

Irrespective of the dip rate, the top and bottom edges of the tablet are subjected to high wall shear stresses at any instant of the reciprocation cycles, but most of the central regions experience comparatively very low shear stresses. In addition, the tablet bottom and top surfaces are subjected to maximum shear stresses midway during the down- and upstrokes, respectively.

Overall, comparisons of the 5 dpm and 10 dpm showed significant quantitative differences in solutions obtained. However, comparison of results between 5 dpm and 5.25 dpm showed that the hydrodynamics is not significantly altered by changes to operational dip rates within the compendial specifications for App 3.

ACKNOWLEDGMENTS AND DISCLOSURES

The authors thank Drs. Narayana Rayapati, Luke Munholand, Genong Li, and Brian Bell from ANSYS, Inc., Lebanon, NH, for their technical support in the development of models. The authors would also like to thank Drs. Stefan Schuber and James Austgen for editorial assistance.

Disclaimer Certain software and hardware are identified in this paper to specify adequately the modeling effort involved. Such identification does not imply approval, endorsement, or certification by USP of the particular brand or product, nor does it imply that the software or hardware is necessarily the best available for the purpose or that any other brand or product was judged to be unsatisfactory or inadequate.

REFERENCES

1. USP. *Fourth Supplement, USP XXII–NF XVII, Drug Release* <724>. Rockville, MD: USP; 1991.
2. USP. *USP 37–NF 32, Dissolution* <711>. Rockville, MD: USP; 2014.
3. Borst I, Ugwu S, Beckett AH. New and extended applications for USP drug release Apparatus 3. Dissolution Technologies. 1997;4: 11–8.
4. McCarthy LG, Kosiol C, Healy AM, Bradley G, Sexton JC, Corrigan OI. Simulating the hydrodynamic conditions in the United States Pharmacopeia paddle dissolution apparatus. AAPS PharmSciTech. 2013;4:83–98.
5. Baxter JL, Kukura J, Muzzio FJ. Hydrodynamics-induced variability in the USP Apparatus II dissolution test. International Journal of Pharmaceutics. 2005;292:17–28.
6. Bai G, Armenante PM. Hydrodynamic, mass transfer and dissolution effects induced by tablet location during dissolution testing. Journal of Pharmaceutical Sciences. 2009;98:1511–31.
7. Kakhi M. Mathematical modeling of the fluid dynamics in the flow-through cell. International Journal of Pharmaceutics. 2009;376:22–40.
8. D'Arcy DM, Liu B, Bradley G, Healy AM, Corrigan OI. Hydrodynamic and species transfer simulations in the USP 4 dissolution apparatus: considerations for dissolution in low velocity pulsing flow. Pharmaceutical Research. 2010;27:246–58.
9. Rohrs BR, Burch-Clark DL, Witt MJ, Stelzer DJ. USP dissolution Apparatus 3 (reciprocating cylinder): instrument parameter effects on drug release from sustained release formulations. Journal of Pharmaceutical Sciences. 1995;84:922–6.
10. Khamanga SMM, Walker RB. The effects of buffer molarity, agitation rate, and mesh size on verapamil release from modified-release mini-tablets using USP Apparatus 3. Dissolution Technologies. 2007;14:19–23.
11. Yu LX, Wang JT, Hussain AS. Evaluation of USP Apparatus 3 for dissolution testing of immediate-release products. AAPS PharmSci. 2002;4:1–5.
12. Sanghvi PP, Nambiar JS, Shukla AJ, Collins CC. Comparison of three dissolution devices for evaluating drug release. Drug Development and Industrial Pharmacy. 1994;20:961–80.
13. Kakhi M. Classification of the flow regimes in the flow-through cell. European Journal of Pharmaceutical Sciences. 2009;37:531–44.
14. Shames IH. Mechanics of fluids. New York: McGraw-Hill Book Company; 1962.
15. ANSYS. ANSYS FLUENT users guide. Release 13.0. Lebanon: ANSYS; 2011.
16. Industrial Perforators Association. The Designers, Specifiers, and Buyers Handbook of Perforated Metals. 1993. http://iperf.org/perforating/knowledge-center/perf-handbook/pressure-loss-through-perforated-plate-air-fluid/. Accessed 2 July 2014.
17. Leslie Controls. Temporary Strainer Technical Information. ND. Available from: www.lesliecontrols.com/Catalogs/cataloglist.cfm, Strainers Handbook (.zip file), Temp Tech Info.pdf. Accessed 2 July 2014.
18. Munson BR, Young DF, Okiishi TH. Fundamentals of Fluid Mechanics. John Wiley & Sons, Inc.; 2006.